First Light from the MAUI Space Experiment

Rainer A. Dressler and Benjamin D. Hester
Air Force Research Laboratory, Space Vehicles Directorate, Hanscom AFB, MA
Paul F. Sydney and Lewis Roberts,
Boeing Corp.
Kris Hamada
Pacific Defense Solutions
Paul Kervin and Mark P. Bolden
Air Force Research Laboratory, Directed Energy Directorate, Kihei, HI
Capt. Albert F. Meza, Darrin T. Walker, and James C. McLeroy
DoD Space Test Program, Johnson Space Center, TX
Lawrence S. Bernstein, James W. Duff, and Matthew Braunstein
Spectral Science, Inc., Burlington, MA

ABSTRACT

The objective of MAUI (Maui Analysis of Upper Atmospheric Injections) is to measure the spatial and spectral properties of Shuttle engine exhaust interactions with the low-Earth orbit environment and to validate the chemical kinetics and transport physics implemented in a direct simulation Monte Carlo (DSMC) computer model, SOCRATES-P. The code is a research tool that can be applied towards the development of a future maneuver characterization capability. MAUI was manifested during the past four Space Shuttle missions. STS-115 resulted in a unique Maui Space Surveillance Site (MSSS) observation opportunity at conditions where the orbiter was in sunlight while MSSS was in darkness (terminator pass). Dedicated MAUI burns were scrubbed due to concern related to an unidentified object in the vicinity of the orbiter. Instead, MSSS was tasked to image the tail section of the orbiter to ensure the object was not the parachute door. STS-115 passed over MSSS in an attitude in which the Shuttle axis was locked to the MSSS line-of-sight. This required a large number of attitude maneuvers. The 0.328° field-of-view LAAT acquisition scope of the 3.6 m telescope of the Advanced Electro-Optical System (AEOS), provided extremely interesting unfiltered imagery in the near-UV visible spectral region of the electromagnetic spectrum. A total of 22 attitude control pulsed firings were recorded at very good lighting conditions. Each firing involved 2 or 3 primary reaction control system (PRCS) engines firing bursts between 80 and 320 ms in duration. In every case, the thrust axis was perpendicular to the line of sight, providing an optimal viewing geometry. By far the most interesting white-light features were transients observed at engine start up and shut-down. These transients are due to droplets, or frozen particles, of un-burnt propellant or condensed exhaust that effectively scatter sunlight. The imagery is such that the velocity of the transients can be accurately determined, thereby providing an excellent opportunity to validate state-of-the-art two-phase flow models implemented in SOCRATES-P. An analysis of the transient speeds based on known PRCS engine start-up and shutdown information will be presented.

1. INTRODUCTION

The MAUI space experiment is a collaborative effort between the AFRL Directed Energy Directorate, the Space Vehicles Directorate, and the DoD Space Test Program (STP) to observe Space Shuttle engine firings from MSSS. The main objective of this effort is to improve our ability to characterize the far-field optical signatures caused by interactions between spacecraft engine exhaust and the low-Earth orbit environment. The shape and volume of the radiation field depends on the atmospheric density, engine type and the maneuver (length of burn, thrust axis angle with respect to spacecraft velocity vector), and solar illumination conditions. MAUI's main technical purpose is to validate a direct simulation Monte Carlo (DSMC) computer model, SOCRATES-P. MAUI addresses a critical need to overcome space object tracking challenges following maneuvers.

MAUI has been manifested as a "payload of opportunity" for Space Shuttle missions STS-121, 115, 116, 117, 118, 120, 122, 123, and 124. MSSS overflight opportunities with MSSS in darkness are considered following Space Shuttle undocking from the International Space Station (ISS). At the time of this report, STS-121, 116, and 117 resulted in no opportunities. First MAUI observations occurred during STS-115 in September, 2006. The single overflight opportunity consisted of a terminator pass during which the Space Shuttle *Atlantis* was in sunlight while

MSSS was in darkness. This was particularly fortunate considering that this experiment occurred close to solar minimum during which atmospheric densities at ISS altitudes are low, resulting in weak optical emissions attributable to exhaust-atmosphere collisions, the main source of radiance in darkness. Observations during solar illumination result in additional interactions that can produce distinct radiance, and we were prepared to investigate those under these unique conditions. Both spectral as well as bandpass filtered imagery were planned. Shortly prior to the overflight, however, the NASA flight controller decided to abandon a dedicated series of Space Shuttle engine burns over MSSS given a concern that arose over an unidentified object flying in the vicinity of the orbiter. NASA feared that the object may be the Shuttle parachute hatch door, and, therefore, requested that MSSS conduct high-resolution imagery of the Shuttle tail section.

The telescopes, therefore, had to be reconfigured, and in the process, filters were removed from the acquisition telescopes used for the planned wide-field-of-view bandpass imagery. However, the requested imagery required that the Space Shuttle be commanded into landmark mode consisting of an attitude with the orbiter aft section pointed toward the MSSS facility. In order to maintain this attitude, frequent pitch, yaw and roll maneuvers were necessary, resulting in a large number of burns. A total of 22 burns were registered using the LAAT acquisition scope on the Advance Electro-Optical System mount at a nominal field of view (FOV) of 0.328° during optimal lighting conditions throughout the first half of the overflight. Each burn involved 2 to 3 primary reaction control system (PRCS) engines, and the thrust axis of the particular engines was in each case perpendicular to the line-of sight due to the highly controlled Shuttle attitude. Although no spectrally resolved data were recorded, the main observed features were transients during engine startup and shutdown. In the present paper, an analysis of these transients using the LAAT video imagery is presented.

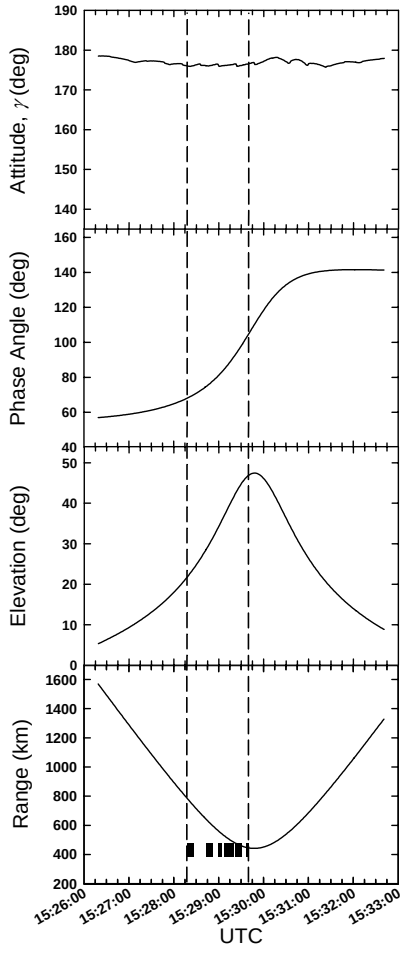

Fig. 1. Range, elevation, solar phase angle and attitude during the Sept. 19, 2006 pass of Atlantis over Maui.

2. EXPERIMENTAL

STS-115, involving the orbiter *Atlantis*, was launched on September 9, 2006. The observation pass of *Atlantis* occurred on September 19, 2006 with culmination with respect to MSSS at 15:29:48 hours (UTC). Fig. 1 provides a summary of pass parameters as a function of time, including range, $\boldsymbol{R}$, elevation, α, solar phase angle, ϕ, and the angle, γ, between the orbiter axis, z, and $\boldsymbol{R}$. The geometry of the experiment and associated parameters are shown schematically in Fig. 2. The Space Shuttle flew over Maui in a landmark mode in which the orbiter z-axis was oriented parallel to the line-of-sight such that high-resolution imagery could be acquired of the Shuttle aft section. A series of attitude maneuvers was necessary to maintain this position. The bottom chart in Fig. 1 provides markers at the time of those attitude control maneuvers that are analyzed in the present paper. The time interval during which burns were analyzed is indicated with vertical dashed lines. After 15:29:40 hours cirrus clouds caused significant background radiation as MSSS approached sunrise, substantially reducing the quality of the observations. The orbiter velocities in the Earth-centered-inertial (ECI) and Earth-centered-fixed (ECF) coordinate systems were 7.715 km/s and 7.42 km/s, respectively. The orbital altitude was 335.15±0.20 km within the time interval of the investigated burns, with $\boldsymbol{R}$ declining from 780 to 446 km during the approach. As is seen in Fig. 1, during the investigated burn interval, the angle, γ, remained constant at a value of 176.3° to within 0.5°. The minor discrepancy with a perfect alignment has minimal bearing on the present analysis.

Wide FOV imagery of the Space Shuttle maintaining axial alignment with the MSSS line of sight was obtained using the LAAT acquisition telescope. This 0.58 m aperture telescope, situated on the AEOS mount, was operated with a nominal FOV of 0.328°. The ICCD detector exhibits sensitivity in the spectral range of 0.4 to 0.9 μm. The gain of the sensor was reduced to limit the size of the spot attributable to saturation by the solar illuminated orbiter hard body. Table 1. lists the pertinent parameters for 22 attitude control burns for

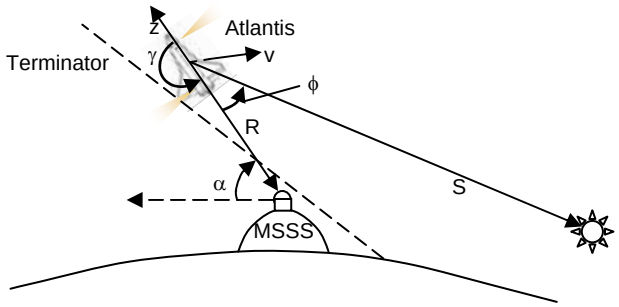

Fig. 2. Schematic representation of the observation geometry.

which quality, 30 frame per second, video footage was obtained. Most of the burns were the minimum burn length of 0.08 s. Burns 2 and 8 were 0.16 s long, while burn 9 was 0.24 s long. 3 types of attitude control maneuvers actuating 2 or 3 primary reaction control system (PRCS) engines were conducted: pitch down, roll left, and yaw right. In the case of the pitch down maneuvers , the F1U, L3D and R3D engines were used, while roll left was caused by the L1U and R3D engines, and yaw right by the F3L and R1R engines. The thrust axis of all of these engines is perpendicular to the Shuttle axis, and, therefore, essentially perpendicular to the line of sight, providing a side-on view of the engine exhaust. A Space Shuttle PRCS engine has a nominal thrust of 3880 N (870 lbf) and uses a monomethyl-hydrazine (MMH) fuel and N_2O_4 oxidizer.

Table 1. also lists the projection, $v_\perp$, of the orbiter ECI velocity vector, **v**, onto the plane normal to the line of sight. This projection is representative of the angular velocity of stars streaking across the FOV as the orbiter is tracked, and is given by:

$$v_\perp = v\sin(\angle\{\mathbf{R},\mathbf{v}\})\,. \tag{1}$$

The dimensions of the video frame at the orbiter altitude can, therefore, be calibrated by determining the velocity of the stars in units of pixels per unit time, from which the scaling factor, distance per pixel, can be derived. At the

Table 1. List of burns analyzed in this work. The velocity projection, $v_\perp$,is the projection of the ECI velocity onto the plane normal to the line of sight. The horizontal frame width, *d*, represents the horizontal dimension of the observed video frame at the distance of the orbiter.

Burn #	UTC	Maneuver	Burn Length (s)	Range (km)	$v_\perp$ (km/s)	*d* (km)
1	15:28:18.993	pitch down	0.08	778.837	4.607	4.976
2	15:28:21.073	yaw right	0.16	766.504	4.670	4.924
3	15:28:25.473	pitch down	0.08	740.743	4.809	4.770
4	15:28:44.593	pitch down	0.08	635.166	5.508	4.137
5	15:28:45.313	pitch down	0.08	631.436	5.537	4.113
6	15:28:48.353	yaw right	0.08	615.922	5.663	3.990
7	15:28:51.073	yaw right	0.12	602.383	5.779	3.914
8	15:29:00.673	pitch down	0.16	557.521	6.203	3.665
9	15:29:02.673	roll left	0.24	548.819	6.294	3.567
10	15:29:03.073	roll left	0.08	547.108	6.312	3.551
11	15:29:08.673	pitch down	0.08	524.242	6.568	3.442
12	15:29:12.193	pitch down	0.08	510.990	6.726	3.342
13	15:29:14.113	roll left	0.08	504.157	6.812	3.257
14	15:29:16.033	roll left	0.08	497.619	6.896	3.251
15	15:29:16.593	yaw right	0.08	495.768	6.920	3.250
16	15:29:18.993	pitch down	0.08	488.141	7.021	3.181
17	15:29:23.713	pitch down	0.08	474.638	7.209	3.105
18	15:29:26.193	roll left	0.08	468.385	7.300	3.067
19	15:29:27.553	roll left	0.08	465.215	7.347	3.088
20	15:29:29.473	pitch down	0.08	461.060	7.410	3.047
21	15:29:38.313	pitch down	0.08	447.029	7.630	2.940
22	15:29:39.073	roll left	0.08	446.231	7.643	2.833

small nominal FOV of 0.328°, it is within the accuracy of the present analysis to assume tan(FOV) ≈ FOV, thereby assuming an image plane. Table 1. lists the derived horizontal frame widths, *d*, at the orbiter distance. From FOV = *d*/*R*, we derive an average FOV of 0.374° for the 22 burns with an excellent standard deviation of 0.004°, thereby confirming a consistent calibration of the observed video imagery.

3. RESULTS

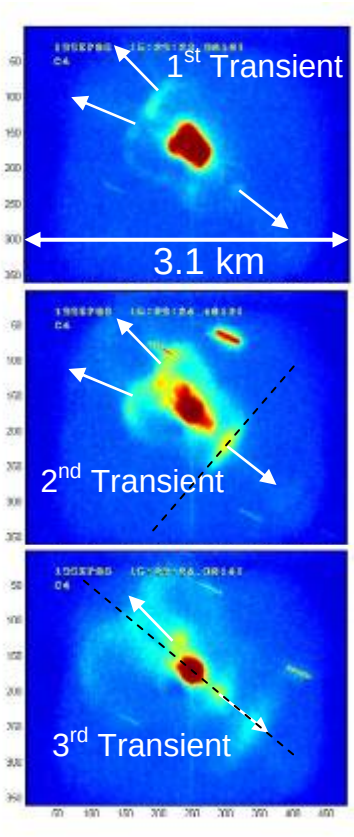

Fig. 3. Video frames taken with the MSSS LAAT acquisition telescope during a 80 ms pitch down maneuver firing. The frames (top to bottom) are separated by 0.2 s.

Close inspection of the video imagery leads to the observation that every burn is accompanied by 3 transients. This is demonstrated for burn 17 in Fig. 3. At this moment of the pass, the horizontal width of the frame corresponds to 3.105 km at the position of the orbiter, which is at the center of the circular region of saturated pixels. Stray light due to the intense sunlight scattered off the body of *Atlantis* caused significant blooming. The sharp streaks are stars, one of which was used for the frame width calibration. Burn 17 was a pitch down burn, which involves the two aft engines, L3D and R3D, firing downward, and the forward engine, F1U, firing upward (towards the bottom right corner of the image). The first transient is the dimmest, and is also readily seen to be the fastest. The second transient is the brightest and most compact, while the third is the slowest and appears to be associated with a trail following the initial burst. As is seen, there is considerable interference between the exhaust of the two aft engines.

The velocities of the individual transients were analyzed for every burn and engine by recording the time dependence of the distance of the center of the respective feature along the thrust axis from the center of the orbiter. A frame by frame analysis establishes that the transient velocities are constant with respect to the distance of the visual center of the feature to the orbiter. The analysis of the velocities is summarized in Table 2, where the average transient velocities are sorted by engine and transient. The global averages of transient velocities averaged over all 22 burns are also provided. There are no noteworthy differences between the engines, the respective average values lying close to the standard deviations of the global average for a respective transient. The first transient has a velocity close to the terminal exhaust velocity of a PRCS engine,[1,2] transient 2 is approximately half the velocity of transient 1, and transient 3 has a velocity that is approximately half that of transient 2. No noticeable trend with time is observed, and, therefore, effects due to engine heating on the terminal velocities can be excluded.

Having derived the velocities of the transients, the time of origin of the transients could be determined. From this determination it becomes clear that transient 1 is associated with engine start up, while transients 2 and 3 are due

Table 2. Axial transient velocities in km/s determined from the analysis of video imagery of attitude control burns, averaged for specific Space Shuttle PRCS engines. Errors correspond to standard deviations.

Engine	Transient 1	Transient 2	Transient 3
F1U	3.268±0.105	1.599±0.067	0.795±0.093
L3D	3.190±0.172	1.686±0.225	0.655±0.143
R3D	3.078±0.170	1.679±0.172	0.701±0.152
F3L	3.093±0.175	1.485±0.097	0.631±0.051
R1R	3.348±0.080	1.392±0.146	0.675±0.090
L1U	2.941±0.205	1.527±0.086	0.713±0.033
Transient Average	**3.132±0.185**	**1.630±0.175**	**0.707±0.128**

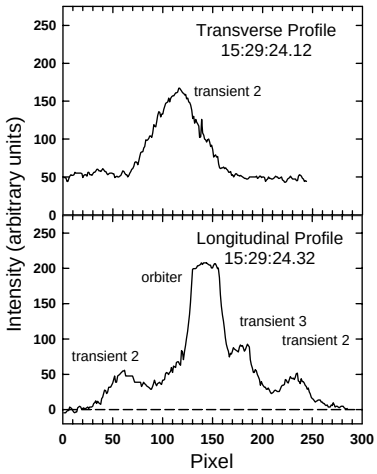

Fig. 4. Intensity profiles of video frames of Fig. 3. Top: 2nd transient profile transverse to thrust axis (dashed line, center frame). Bottom: Profile along thrust axis (dashed line bottom frame).

to engine shutdown as they have times of origin that are delayed by the burn times reported to us by NASA. In order to derive clues with respect to the source of the transient signatures, the evolution of the integrated intensity of a transient is examined. This was primarily conducted for transient 2 since it is the most intense. Prior to integrating the intensities of the transient for a particular frame, the average background level is determined by taking a profile along a line through the transient that is perpendicular to the thrust axis. This is demonstrated in Fig. 4 for burn 17, where the top chart shows a profile transverse to the thrust axis of the 2nd transient of the F1U engine (see dashed line in middle chart in Fig. 3). It is seen that the background level is approximately 47 units at both ends of the feature. Some additional spurious signal is also visible at the low pixel end, which contributes to the uncertainty in the determination of the integrated feature intensity.

The bottom chart in Fig. 4 is a profile along the thrust axis of the F1U engine taken from the bottom frame of Fig. 3. The profile has been corrected for background signal, as determined from the frame of the top chart. The orbiter presents the most intense, saturated feature around 200 intensity units. The intensity scale spans 256 units, and a nonlinear intensity regime must be assumed as maximum intensity is approached. Both the 2nd and 3rd transients of the F1U engine are observable at the high pixel end. It is also apparent that there is some overlap between the two features. At the low pixel side of the orbiter, the 2nd transient from the two aft engines is also visible. It is slightly closer to the orbiter, as the profile is taken along a line off axis with respect to the two engines which are canted at ~10° with respect to each other.

Figure 5 shows the dependence of the integrated intensity of the 2nd transient as a function of time following engine shutdown for the F1U engine in pitch down maneuvers 1 and 17. The intensity was determined following background subtraction by defining the image area of the transient with a polygon. The intensities are normalized with respect to the range (R^2) and atmospheric transmission. In case of the latter, an average wavelength of 600 nm was assumed. After ~0.5 s, the integrated intensity declines with time. Prior to 0.5 s, the intensity appears to be constant or rising with time. Examination of the individual pixel intensities indicates that in the case of burn 1, no pixels registered intensities exceeding 200 units prior to background subtraction, while in the case of burn 17, no pixels had intensities exceeding 210 units beyond 0.3 s. It can, therefore, be concluded that saturation and non-linearity in the CCD response are most likely not the source of the varying time dependence of the integrated intensity of the 2nd transient.

Figure 6 shows the evolution of the of the F1U engine 2nd transient intensity from burn to burn during the pass. The intensity, taken at 0.6 s after shutdown, is plotted versus the solar scattering angle, $\varphi = 180° - \phi$. As in Fig. 5, the intensities were normalized with respect to the range and the atmospheric transmission. The solar zenith angle decreases from ~103.3 to 99.5° during the burn sequence. At 103.3°, the tangent height is at its lowest altitude of 149.5 km, and atmospheric scattering through the Earth limb can, therefore, be neglected. The solar scattering angle for burn 1 is 111.5° and declines to φ = 76° at burn 17. A minor increase in intensity with solar scattering is observed.

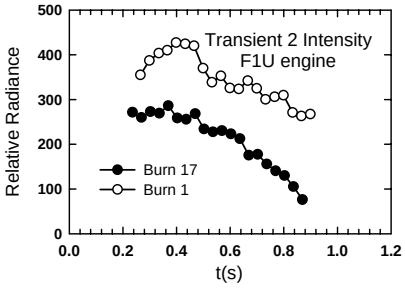

Fig. 5. Range and transmission normalized intensity versus time following engine shutdown for F1U 2nd transients.

4. DISCUSSION

Previous information on optical signatures during sunlit Space Shuttle engine burns was obtained during the GLO experiments[3-5] in which an imager/spectrograph was flown in the bay of the orbiter and spectral measurements of far-field engine exhaust radiance were recorded. Fig. 7 shows examples of optical spectra acquired during the GLO-2 mission on STS-63 that flew in February of 1995. The spectra of a 3 s PRCS burn were recorded in sunlight with 2 s long

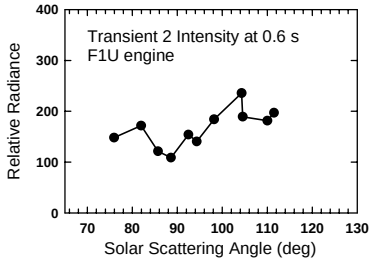

Fig. 6. 2nd transient intensity 0.6 s after shutdown as a function of solar scattering angle. The intensity is range and transmission normalized.

exposures. The instrument line of sight was aligned with the engine thrust axis. The bottom spectrum was measured during the burn, where spectral features due to OH, NO, and NH are readily identified. The top spectrum is recorded approximately 3 s following the burn, and exhibits a broad background with increasing intensity with wavelength. The two sharp intensity dips at ~393 and 397 nm are the well known Ca II K and H lines observed in the solar spectrum. It can, therefore, be concluded that the top spectrum is due to solar scatter from droplets or particulates in the exhaust. The solar scatter intensity rapidly dims in the first seconds following the end of the burn, and then declines at a lower rate past 10 s. This observation is consistent with the interpretation that the solar scatter is associated with transients 2 and 3 that we associate with engine shutdown. While the sharp drop in intensity can be related to transient 2 that recoils from the orbiter with a higher velocity, the slow decline must be associated with the trails of the slower transient 3.

Previous observations of solar scatter in association with Space Shuttle experiments involved the observation of a water venting during a similar terminator pass over AMOS.[6] In that case, the far-field solar scatter was primarily associated with scattering from sub-micron sized particles formed by recondensation of water sublimated from larger ice particles formed near the venting orifice. The present engine transients are most likely formed by droplets or particles as well. The high velocity of transient 1, formed at engine start up, suggests that this transient may be attributable to exhaust condensation. This, however, would imply that the solar scatter would be observable throughout the burn, which is not the case as demonstrated by the bottom spectrum in Fig. 7. Alternatively, it is conceivable that at engine start-up, mixing of oxidizer and fuel are not complete, leading to unburned droplets that take on the velocity of the exhaust through collisional drag forces. The incomplete mixing can be attributed to the different volatilities of the oxidizer and fuel, leading to an earlier appearance of the oxidizer in the combustion chamber due to its higher vapor pressure. The vapor pressure of N_2O_4 and MMH are 96 and 4.9 kPa, respectively, at 20°C.

The shutdown transients can be associated with oxidizer and fuel present in the vacuum manifold between the tank valves and the combustion chamber. When the oxidizer and fuel valves are turned off simultaneously, the oxidizer and fuel in the vacuum manifold are no longer pressurized. The more volatile oxidizer can then be expected to vent into the combustion chamber more rapidly than the fuel, which is also considerably more viscous. This interpretation implies that transient 2 is due to droplets of frozen particles of the oxidizer, while transient 3 is attributable to the MMH fuel.

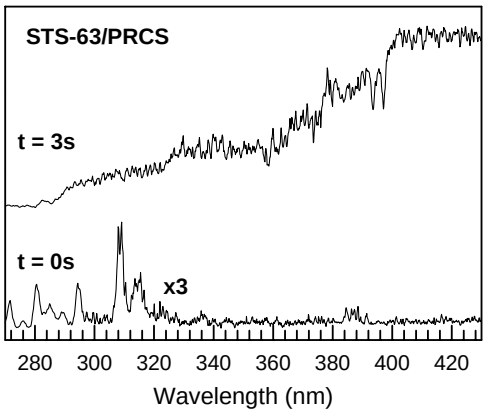

Fig. 7. GLO spectra of exhaust far-field radiance during (t = 0) and after a 3 s PRCS burn in daylight.

The size of the droplets or particles dictates the scattering intensities and may affect the transient velocities. The latter, listed in Table 2, result from combustion gas interaction with the condensed phase. In case of very small particles or droplets, they can be expected to take on the terminal velocity of the exhaust gases. A module has recently been incorporated in the SOCRATES-P spacecraft interactions code, developed by AFRL and Spectral Sciences Inc., that computes the multi-phase interaction. Assuming full gas accommodation, the model determines that particles of 0.1 μm radius experience no velocity slip, while 1 and 10 μm radius particles reach asymptotic velocities of 2,850 and 2,100 m/s, respectively. In the case of the startup transient (1st transient), the droplets have essentially the terminal velocity of the exhaust gases in the collisionless regime. This transient can be associated with not optimally mixed fuel and oxidizer during the engine startup phase. The surviving fuel and/or oxidizer droplets are then "pushed" by the exhaust of efficiently burned propellant.

In the case of the shutdown transients, the lower velocities do not have a simple explanation. If the second transient is due to submicron particle radii, the terminal velocity of ~1.6 km/s can be interpreted to arise from the very lean propellant mixture at shutdown, leading to a lower temperature expansion. The associated exhaust gases accelerate the oxidizer droplets to lower velocities than those produced at optimal combustion conditions.

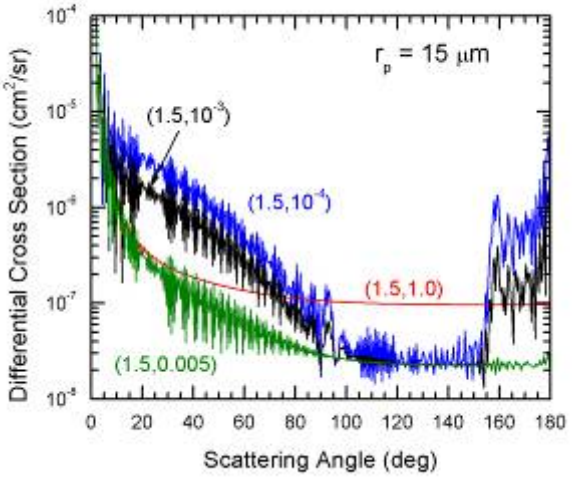

Fig. 8. Mie scattering cross section calculations for a 15 μm radius N_2O_4 particle and different imaginary refractive indices (second number in parentheses) at 600 nm.

Alternately, if the oxidizer droplets expelled at shutdown have radii exceeding 10 μm, they experience significant velocity slip. The less volatile fuel is expelled later and closer to the moment of complete shutdown, which is consistent with the lowest velocity among the three transients irrespective of the associated particle size.

The absolute solar scattering intensities, following corrections with respect to atmospheric transmission and range, are a function of Mie-scattering cross sections. The absolute cross sections and their angular dependence depend on the size and the complex refractive index of the particles. In case of the oxidizer, optical refractive properties are not available below 1 μm. The real component varies slowly with wavelength over its known range and it is reasonable to assume that the value at 1 μm applies to the visible region. However, the imaginary component is strongly affected by absorption features. From the NO_2 absorption cross section at 600 nm, we estimate the refractive index of N_2O_4 to be 1.5 + 0.005i.

Fig. 8 compares Mie scattering cross sections for different imaginary refractive indices of a 15 μm radius droplet. It is seen that the cross sections become less dependent on angle between 75 and 120° as the imaginary refractive index increases. While the absolute values change rapidly with particle size, we do not find that the angular dependence varies strongly with size. The range of solar scattering angles in Fig. 6 is too narrow to make an assessment on the size distribution of the droplets or particles based on the intensity distribution. However, there does appear to be an increase in the normalized intensity with angle, counter to Mie scattering predictions. This could be an indication that the particles are significantly smaller.

The derivation of absolute radiance intensities, currently in progress, will be more helpful in characterizing the average size of the solar-scattered matter. The integrated intensity scattered from the cloud at angle, φ, is given by:

$$I(\varphi) = \int_0^\infty d\lambda\, g(\lambda) I_S(\lambda) \int_0^\infty dr\, f(r)\sigma(\lambda, r, \varphi) \tag{2}$$

Where $g(\lambda)$ incorporates the spectral atmospheric transmission and sensor sensitivity, $I_s(\lambda)$, is the solar flux at wavelength, λ, $\sigma(\lambda,r,\varphi)$ is the Mie scattering cross section, and $f(r)$ is the normalized size distribution for radii, r, per unit length, where the number of oxidizer droplets or particles, N_{ox}, is given by:

$$N_{ox} = \int_0^\infty f(r)dr\ . \tag{3}$$

The absolute magnitude of $\sigma(\lambda,r,\varphi)$ is proportional to r^2 for size parameters $2\pi r/\lambda >> 1$ (geometric scattering), while for $2\pi r/\lambda <\sim 3$, the cross section is proportional to r^6. Assuming that $f(r)$ is a delta-function, Eq. (3) can be rewritten:

$$N_{ox} = \frac{3V_{ox}}{4\pi r^3}, \tag{4}$$

where V_{ox} is the volume of the condensed phase oxidizer. It is seen from Eq. (4) that in the case of droplets with average radii in the geometric regime, the intensity scales with r^{-1}, while for droplets with average radii in the Rayleigh regime, the intensity scales to r^3. Thus, if the droplets or particles are in the Rayleigh regime, the intensity is particularly sensitive to evaporative losses. The transition to the Rayleigh regime was identified in the water venting studies, where scattering from water ice particles was observed for significantly longer times following release than in the present study with narrower field of view.[6]

The time evolution of the intensity of a single transient in the present study may, therefore, provide information on the particle size. Examples of the time evolution of the oxidizer transient are shown in Fig. 5. In the previous water venting study by Kofsky et al.,[6] water droplets cooled evaporatively within ~0.5 s to a more stable temperature of 180 K. Subsequently, evaporative and emissive energy losses were balanced by solar and earthshine absorption.

Eventually, a rapid reduction in ice particle radius occurred. Attempts to model the evolution led to the conclusion that significant surface roughening reduced the albedo of the particles. Preliminary calculations using the methodology of Kofsky et al.[6] show similar behavior of the oxidizer cloud particles (transient 2) with more rapid evaporation and cooling given the substantially higher vapor pressure of the oxidizer. The N_2O_4 condensates can thus also be expected to be in the solid phase given the relatively high melting point of 262 K. 1 μm and smaller particles exhibit a significant decline in radius after 0.5 s, consistent with the observed decline in integrated intensity.

The present characterization of one startup and two shutdown transients of the Shuttle PRCS bipropellant engine is extremely valuable in terms of interpreting other observations of Shuttle engine burns. In experiments on STS-33,[7] transients were also observed after dedicated burns during night passes over AMOS. The signatures are attributable to chemiluminescence associated with the interaction of the transient condensed and vapor phases with the thermosphere, primarily atomic oxygen. From the derivation of the velocity of the transients at night, the observed luminescence can be attributed either to oxidizer or fuel chemiluminescence, the intensity of which is found to depend on the thrust axis orientation with respect to the velocity vector. Meanwhile, an analysis of the startup chemiluminescence front in that experiment produces a velocity with respect to the spacecraft that is essentially identical to the presently determined startup transient velocity.

5. CONCLUSIONS

First data were acquired as part of the MAUI space experiment during the STS-115 mission. Successful measurements of Space Shuttle attitude control firings were obtained during a terminator pass. These represent first ground-based recordings of Shuttle engine firings with the orbiter in sunlight. 22 short burns were observed, the most prominent features of which were transients attributable to incomplete combustion products, expelled in condensed form, at engine startup and shutdown. The most intense transient was attributable to pure oxidizer released at shutdown. The startup transient has a velocity with respect to the spacecraft that is comparable to the terminal velocity of exhaust gases. The oxidizer and fuel transients exhibit average velocities of 1.63±0.18 and 0.71±0.13 km/s, respectively. The spatially integrated intensity of the oxidizer transient is nearly constant with time up to 0.5 s after shutdown, following which the intensity begins to decline.

ACKNOWLEDGMENTS

This work has been initiated and partially funded by AFOSR under tasks 2301HS 02VS06 (program manager: Kent Miller). Some of us have been supported by the Common High Performance Computer Software Support Initiative (CHSSI) High Performance Computer Modernization Office, managed by Tom Smith (AFRL/PRS).

[1] J. S. Pickett, G. R. Murphy, W. S. Kurth, C. K. Goertz, and S. D. Shawhan, J. Geophys. Res. 90, 3487, 1985.
[2] Rodney A. Viereck, Lawrence S. Bernstein, Stephen B. Mende, Edmond Murad, Gary R. Swenson, and Charles P. Pike, Journal of Spacecraft and Rockets 30, 724, 1993.
[3] A. L. Broadfoot, B. R. Sandel, D. J. Knecht, R. A. Viereck, and E. Murad, Appl. Opt. 31, 3083, 1992.
[4] L. S. Bernstein, Y. Chiu, A. Gardner J, A. L. Broadfoot, M. I. Lester, M. Tsiouris, R. A. Dressler, and E. Murad, J. Phys. Chem. A 107, 10695, 2003.
[5] L. S. Bernstein, M. Braunstein, A. L. Broadfoot, W. L. Dimpfl, R. A. Dressler, Y.-h. Chiu, J. A. Gardner, and E. Murad, J. of Spacecraft and Rockets 43, 1370, 2006.
[6] I. L. Kofsky, D. L. A. Rall, M. A. Maris, N. H. Tran, E. Murad, C. P. Pike, D. J. Knecht, R. A. Viereck, A. T. Stair Jr, and A. Setayeh, Acta Astronautica 26, 325, 1992.
[7] D. L. A. Rall, I. L. Kofsky, C. P. Pike, D. J. Knecht, and T. P. Zehnpfennig, J. Spacecraft and Rockets 33, 393, 1996.